PHYSICAL REVIEW B **87**, 174427 (2013)

Topological chiral magnonic edge mode in a magnonic crystal

Ryuichi Shindou,[*] Ryo Matsumoto, and Shuichi Murakami
Department of Physics, Tokyo Institute of Technology, 2-12-1 Ookayama, Meguro-ku, Tokyo, Japan

Jun-ichiro Ohe
Department of Physics, Toho University, 2-2-1 Miyama, Funabashi, Chiba, Japan

(Received 6 April 2013; published 24 May 2013)

Topological phases have been explored in various fields in physics such as spintronics, photonics, liquid helium, correlated electron system, and cold-atomic system. This leads to the recent foundation of emerging materials such as topological band insulators, topological photonic crystals, and topological superconductors/superfluid. In this paper, we propose a topological magnonic crystal which provides protected chiral edge modes for magnetostatic spin waves. Based on a linearized Landau-Lifshitz equation, we show that a magnonic crystal with the dipolar interaction acquires a spin-wave volume-mode band with nonzero Chern integer. We argue that such magnonic systems are accompanied by the same integer numbers of chiral spin-wave edge modes within a band gap for the volume-mode bands. In these edge modes, the spin wave propagates in a unidirectional manner without being scattered backward, which implements novel fault-tolerant spintronic devices.

DOI: 10.1103/PhysRevB.87.174427 PACS number(s): 85.75.−d, 73.43.−f, 03.65.Vf, 85.70.Ec

I. INTRODUCTION

Topological phases in condensed matters have been attracting much attention because of their fascinating physical properties. Discoveries of topological band insulators[1–7] open up an emerging research paradigm on spin-orbit interaction physics. Relativistic spin-orbit interaction in the topological band insulator endows its Bloch electron bands with nontrivial global phase structures, which leads to novel surface metallic states.[5,8] Superconductor analogs of topological insulators have exotic edge modes,[9,10] which are composed only of Majorana fermion. Some aspects of these bound states are experimentally confirmed,[11,12] fostering much prospect of the realization of quantum computers.[13] A photonics analog of quantum Hall phase with chiral edge modes is proposed theoretically[14–16] and is subsequently designed in actual photonics crystals.[17] Unidirectional propagations of an electromagnetic wave along these edge modes were experimentally observed, which provides these metamaterials with unique photonic functionality.

In this paper, we theoretically propose a spin-wave analog of topological phases, which has a topologically protected chiral edge mode for the spin-wave propagation. The spin wave is a collective propagation of precessional motions of magnetic moments in magnets. Depending on its wavelength, spin waves are classified into two categories. One is the exchange spin wave with the shorter wavelength, whose motion is driven by the quantum-mechanical exchange interactions ("exchange-dominated" region). The other is the magnetostatic spin wave with the longer wavelength,[18,19] whose propagation is caused by the long-range dipolar interaction ("dipolar" region). Magnonics research investigates how these spin waves propagate in the submicrometer length scale and subnanosecond time scale.[20–22] Like in other solid-state technologies such as photonics and plasmonics, the main application direction is to explore the ability of the spin wave to carry and process information. Especially, the propagation of spin waves in periodically modulated magnetic materials dubbed as magnonic crystals[22–32] is one of its central concerns. Owing to the periodic structuring, the spin-wave volume-mode spectrum in magnonic crystal acquires allowed frequency bands of spin-wave states and forbidden-frequency bands (band gap).[22–30]

In the next section, we introduce a topological Chern number in these volume-mode bands with a band gap. In Sec. III, we consider a two-dimensional magnonic crystal (MC), where the Chern number for the lowest spin-wave volume mode takes nonzero integer values in the dipolar region. In Sec. IV, we argue that the nonzero Chern integer for the lowest volume-mode band results in the same integer numbers of topological chiral edge modes (surface modes; Fig. 1), whose dispersions run across the band gap between the lowest volume-mode band and the second lowest volume-mode band. The existence of the topological chiral edge mode in the MC is further justified by a micromagnetic simulation in Sec. V. The relevant length scale for the magnonic crystal turns out to be from sub-μm to sub-mm, well within the range of nanosize fabrication. Unidirectional propagations of spin waves along the edge modes are experimentally measurable especially in yttrium iron garnet (YIG), where the coherence length of magnons is on the order of centimeters.[21] Based on these observations, we argue in Sec. VI that the topological chiral edge modes can be easily channelized, twisted, split, and manipulated, which enables us to construct novel magnonic devices such as spin-wave logic gate and spin-wave current splitter.

II. CHERN NUMBER IN BOSON SYSTEMS

A. Bosonic BdG Hamiltonian

To introduce the topological Chern number for the spin-wave volume-mode band, we first consider a quadratic form of generic boson Hamiltonian,

$$\hat{\mathcal{H}} = \frac{1}{2}\sum_{\boldsymbol{k}}[\boldsymbol{\beta}^{\dagger}_{\boldsymbol{k}}\ \boldsymbol{\beta}_{-\boldsymbol{k}}] \cdot \boldsymbol{H}_{\boldsymbol{k}} \cdot \begin{bmatrix} \boldsymbol{\beta}_{\boldsymbol{k}} \\ \boldsymbol{\beta}^{\dagger}_{-\boldsymbol{k}} \end{bmatrix}, \tag{1}$$

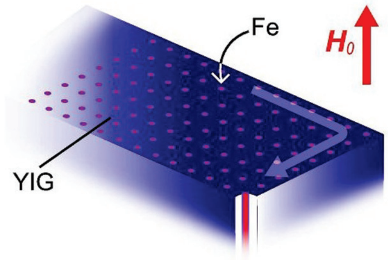

FIG. 1. (Color online) Magnonic crystal with chiral edge modes. Periodic array of holes is introduced into YIG, where iron (Fe) is filled inside every hole. Chiral spin-wave edge modes are propagating along the boundary in a unidirectional way (light purple arrow).

where $\boldsymbol{\beta}_{\boldsymbol{k}}^{\dagger} \equiv [\beta_{1,\boldsymbol{k}}^{\dagger},\ldots,\beta_{N,\boldsymbol{k}}^{\dagger}]$ denote spin-wave (boson) creation operators. Describing volume-type modes, the operators are already Fourier-transformed in a two-dimensional space with the periodic boundary conditions and the wave vector $\boldsymbol{k} \equiv (k_x,k_y)$. N is a number of internal degrees of freedom considered within a unit cell. A $2N$ by $2N$ Hermitian matrix ($\boldsymbol{H}_{\boldsymbol{k}}$) stands for a bosonic Bogoliubov–de Gennes (BdG) Hamiltonian, whose explicit form will be derived from a linearized Landau-Lifshitz equation later. With the magnetic dipolar interaction, the Hamiltonian thus derived acquires not only N by N normal parts (particle-hole channel), $\boldsymbol{a}_{\boldsymbol{k}}$ and $\boldsymbol{a}^*_{-\boldsymbol{k}}$, but also N by N anomalous parts (particle-particle channel), $\boldsymbol{b}_{\boldsymbol{k}}$ and $\boldsymbol{b}^*_{-\boldsymbol{k}}$,

$$\boldsymbol{H}_{\boldsymbol{k}} \equiv \begin{bmatrix} \boldsymbol{a}_{\boldsymbol{k}} & \boldsymbol{b}_{\boldsymbol{k}} \\ \boldsymbol{b}^*_{-\boldsymbol{k}} & \boldsymbol{a}^*_{-\boldsymbol{k}} \end{bmatrix}.$$

Such a bosonic BdG Hamiltonian is diagonalized in terms of a paraunitary matrix $\boldsymbol{T}_{\boldsymbol{k}}$ instead of a unitary matrix,[33]

$$\boldsymbol{T}_{\boldsymbol{k}}^{\dagger}\boldsymbol{H}_{\boldsymbol{k}}\boldsymbol{T}_{\boldsymbol{k}} = \begin{bmatrix} \boldsymbol{E}_{\boldsymbol{k}} & \\ & \boldsymbol{E}_{-\boldsymbol{k}} \end{bmatrix}, \tag{2}$$

with $[\boldsymbol{\gamma}_{\boldsymbol{k}}^{\dagger},\boldsymbol{\gamma}_{-\boldsymbol{k}}]\boldsymbol{T}_{\boldsymbol{k}}^{\dagger} = [\boldsymbol{\beta}_{\boldsymbol{k}}^{\dagger},\boldsymbol{\beta}_{-\boldsymbol{k}}]$. $\boldsymbol{E}_{\boldsymbol{k}}$ is a diagonal matrix, whose diagonal element gives a dispersion relation for respective volume-mode band. The orthogonality and completeness of a new basis ($\boldsymbol{\gamma}$ field) are derived as

$$\boldsymbol{T}_{\boldsymbol{k}}^{\dagger}\boldsymbol{\sigma}_3\boldsymbol{T}_{\boldsymbol{k}} = \boldsymbol{\sigma}_3,\, \boldsymbol{T}_{\boldsymbol{k}}\boldsymbol{\sigma}_3\boldsymbol{T}_{\boldsymbol{k}}^{\dagger} = \boldsymbol{\sigma}_3, \tag{3}$$

respectively, where a diagonal matrix $\boldsymbol{\sigma}_3$ takes ± 1 in the particle/hole space, i.e., $[\boldsymbol{\sigma}_3]_{jm} = \delta_{jm}\sigma_j$ with $\sigma_j = +1$ for $j = 1,\ldots,N$ and $\sigma_j = -1$ for $j = N+1,\ldots,2N$. This additional structure comes from the fact that the magnon obeys the boson statistics. Each column vector encoded in the paraunitary matrix $\boldsymbol{T}_{\boldsymbol{k}}$ stands for the (periodic part of) Bloch wave function for the respective volume-mode band.

Provided that a Hermite matrix $\boldsymbol{H}_{\boldsymbol{k}}$ is unitarily equivalent to a positive-definite diagonal matrix, a paraunitary matrix $\boldsymbol{T}_{\boldsymbol{k}}$ which diagonalizes $\boldsymbol{H}_{\boldsymbol{k}}$ can be obtained by a method based on the Cholesky decomposition.[33] In the method, we first decompose $\boldsymbol{H}_{\boldsymbol{k}}$ into a product between an upper triangle matrix $\boldsymbol{K}_{\boldsymbol{k}}$ and its Hermite conjugate, $\boldsymbol{H}_{\boldsymbol{k}} = \boldsymbol{K}_{\boldsymbol{k}}^{\dagger}\boldsymbol{K}_{\boldsymbol{k}}$. The unitarily positive definiteness of $\boldsymbol{H}_{\boldsymbol{k}}$ always allows this decomposition and also guarantees the existence of $\boldsymbol{K}_{\boldsymbol{k}}^{-1}$. We next introduce a unitary matrix $\boldsymbol{U}_{\boldsymbol{k}}$ which diagonalizes a Hermite matrix

$$\boldsymbol{W}_{\boldsymbol{k}} \equiv \boldsymbol{K}_{\boldsymbol{k}}\boldsymbol{\sigma}_3\boldsymbol{K}_{\boldsymbol{k}}^{\dagger},$$

$$\boldsymbol{U}_{\boldsymbol{k}}^{\dagger}\boldsymbol{W}_{\boldsymbol{k}}\boldsymbol{U}_{\boldsymbol{k}} = \begin{bmatrix} \boldsymbol{E}_{\boldsymbol{k}} & \\ & -\boldsymbol{E}_{-\boldsymbol{k}} \end{bmatrix}.$$

Owing to Sylvester's law of inertia, both $\boldsymbol{E}_{\boldsymbol{k}}$ and $\boldsymbol{E}_{-\boldsymbol{k}}$ can be made positive-definite N by N diagonal matrices. One can see *a posteriori* that these two diagonal matrices are nothing but those in the right-hand side of Eq. (2). Namely, the following paraunitary matrix satisfies Eq. (3):[33]

$$\boldsymbol{T}_{\boldsymbol{k}} = \boldsymbol{K}_{\boldsymbol{k}}^{-1}\boldsymbol{U}_{\boldsymbol{k}}\begin{bmatrix} \boldsymbol{E}_{\boldsymbol{k}}^{1/2} & \\ & \boldsymbol{E}_{-\boldsymbol{k}}^{1/2} \end{bmatrix} \tag{4}$$

and it diagonalizes the Hamiltonian as

$$\boldsymbol{H}_{\boldsymbol{k}}\boldsymbol{T}_{\boldsymbol{k}} = \boldsymbol{\sigma}_3\boldsymbol{T}_{\boldsymbol{k}}\begin{bmatrix} \boldsymbol{E}_{\boldsymbol{k}} & \\ & -\boldsymbol{E}_{-\boldsymbol{k}} \end{bmatrix}. \tag{5}$$

The upper N by N diagonal matrix in the right-hand side, $\boldsymbol{E}_{\boldsymbol{k}}$, is positive definite, so we will refer to them as (dispersions for) "particle bands," while the lower N by N diagonal matrix, $-\boldsymbol{E}_{-\boldsymbol{k}}$, is negative definite, whose diagonal elements are thus referred to as (dispersion for) "hole bands." Due to the trivial redundancy, $\boldsymbol{\sigma}_1\boldsymbol{H}_{\boldsymbol{k}}^*\boldsymbol{\sigma}_1 = \boldsymbol{H}_{-\boldsymbol{k}}$ with $[\boldsymbol{\sigma}_1]_{jm} = \delta_{|j-m|,N}$, either one of these two N by N diagonal matrices gives the full information of the dispersions for the volume-mode bands.

B. Chern integers in bosonic BdG systems

To introduce the Chern number for the jth volume-mode band, let us first define a projection operator P_j in the $2N$-dimensional vector space, which filters out those bands other than the jth volume-mode band at each momentum point $\boldsymbol{k}$,

$$\boldsymbol{P}_j \equiv \boldsymbol{T}_{\boldsymbol{k}}\boldsymbol{\Gamma}_j\boldsymbol{\sigma}_3\boldsymbol{T}_{\boldsymbol{k}}^{\dagger}\boldsymbol{\sigma}_3. \tag{6}$$

Here $\boldsymbol{\Gamma}_j$ is a diagonal matrix taking $+1$ for the jth diagonal component and zero otherwise. Equation (3) suggests that the operator obeys $\sum_j \boldsymbol{P}_j = \boldsymbol{1}$ and $\boldsymbol{P}_j\boldsymbol{P}_m = \delta_{jm}\boldsymbol{P}_j$. In terms of the projection operator, the Chern number for the jth band is given as follows:[34]

$$C_j \equiv \frac{i\epsilon_{\mu\nu}}{2\pi}\int_{\mathrm{BZ}} d\boldsymbol{k}\,\mathrm{Tr}[(\boldsymbol{1}-\boldsymbol{P}_j)(\partial_{k_\mu}\boldsymbol{P}_j)(\partial_{k_\nu}\boldsymbol{P}_j)], \tag{7}$$

where the integral is over the first Brillouin zone (BZ) in the two-dimensional $\boldsymbol{k}$ space.

Equation (7) is integer-valued and characterizes a certain global phase structure associated with a Bloch wave function over the BZ. To see this, we follow the same argument as in the quantum Hall case,[35,36] and introduce field strength (Berry's curvature) B_j and gauge connection (gauge field) $(A_{j,x},A_{j,y})$ for each volume-mode band,

$$B_j(\boldsymbol{k}) \equiv \partial_{k_x}A_{j,y}(\boldsymbol{k}) - \partial_{k_y}A_{j,x}(\boldsymbol{k}), \tag{8}$$

$$A_{j,\nu}(\boldsymbol{k}) \equiv i\,\mathrm{Tr}[\boldsymbol{\Gamma}_j\boldsymbol{\sigma}_3\boldsymbol{T}_{\boldsymbol{k}}^{\dagger}\boldsymbol{\sigma}_3(\partial_{k_\nu}\boldsymbol{T}_{\boldsymbol{k}})], \tag{9}$$

with $j = 1,\ldots,2N$. The Chern number for a volume-mode band reduces to an integral of the respective Berry's curvature over the BZ,

$$C_j = \frac{1}{2\pi}\int_{\mathrm{BZ}} d^2\boldsymbol{k}\,B_j(\boldsymbol{k}). \tag{10}$$

Such a surface integral is zero, provided that the respective gauge field can be defined uniquely and smoothly over the first BZ. When $[\boldsymbol{T}_{\boldsymbol{k}}]_{m,j}$ has a zero somewhere on the BZ for any m ($m = 1,\ldots,2N$), however, the gauge field for the jth band cannot be chosen uniquely over the BZ. In this case, it is necessary to decompose the BZ into two overlapped regions (H_1 and H_2 with $H_1 \cup H_2 = \mathrm{BZ}$ and $H_1 \cap H_2 = \partial H_1 = -\partial H_2 \equiv S$), so that $[\boldsymbol{T}_{\boldsymbol{k}}]_{1,j}$ does not have any zero within one region (H_1), while $[\boldsymbol{T}_{\boldsymbol{k}}]_{2,j}$ has no zero inside the other (H_2). In the former region, we then take the gauge, $[\boldsymbol{T}^{(1)}_{\boldsymbol{k}}]_{m,j}$, such that $[\boldsymbol{T}^{(1)}_{\boldsymbol{k}}]_{1,j}$ is always real positive, while we take another gauge in the other, making $[\boldsymbol{T}^{(2)}_{\boldsymbol{k}}]_{2,j}$ to be always real positive. Provided that the jth band considered is isolated from the others ($E_{\boldsymbol{k},j} \neq E_{\boldsymbol{k},m\neq j}$ for any $\boldsymbol{k}$), these two gauge choices are related to each other by a U(1) transformation,

$$\boldsymbol{T}^{(2)}_{\boldsymbol{k}}\boldsymbol{\Gamma}_j = \boldsymbol{T}^{(1)}_{\boldsymbol{k}}\boldsymbol{\Gamma}_j e^{i\theta_{\boldsymbol{k}}}, \tag{11}$$

on $\boldsymbol{k} \in H_1 \cap H_2$. Now that the gauge of $\boldsymbol{T}^{(1)}_{\boldsymbol{k}}\boldsymbol{\Gamma}_j$ and the gauge of $\boldsymbol{T}^{(2)}_{\boldsymbol{k}}\boldsymbol{\Gamma}_j$ are uniquely defined in H_1 and H_2, respectively,

$$A^{(m)}_{j,\nu} \equiv i\mathrm{Tr}\big[\boldsymbol{\Gamma}_j\boldsymbol{\sigma}_3\boldsymbol{T}^{(m)\dagger}_{\boldsymbol{k}}\boldsymbol{\sigma}_3\big(\partial_{k_\nu}\boldsymbol{T}^{(m)}_{\boldsymbol{k}}\big)\big] \tag{12}$$

($m = 1,2$) are smooth functions in each of these two regions, respectively. The Stokes theorem is applied separately, so that Eq. (10) is calculated as

$$C_j = \frac{1}{2\pi}\oint_S d\boldsymbol{k}\cdot\big(A^{(1)}_j - A^{(2)}_j\big) = \frac{1}{2\pi}\oint_S d\boldsymbol{k}\cdot\nabla_{\boldsymbol{k}}\theta_{\boldsymbol{k}}, \tag{13}$$

with $\nabla_{\boldsymbol{k}} \equiv (\partial_{k_x},\partial_{k_y})$. Two regions share a boundary (S), which forms a closed loop. $\theta_{\boldsymbol{k}}$ in Eq. (11) has a $2\pi n$ phase winding along the loop. This leads to $C_j = n$ ($n = \mathbb{Z}$).

C. Sum rule for Chern integer

When all volume-mode bands in a system are physically stable, the sum of the Chern integer over all particle bands and that over all hole bands are zero, respectively,

$$\sum_{j=1}^{N} C_j = \sum_{j=N+1}^{2N} C_j = 0. \tag{14}$$

To see this, let us linearly interpolate a $2N$ by $2N$ spin-wave Hamiltonian and the $2N$ by $2N$ unit matrix,

$$\boldsymbol{H}_{\boldsymbol{k},\lambda} = (1-\lambda)\boldsymbol{H}_{\boldsymbol{k}} + \lambda\boldsymbol{1}. \tag{15}$$

We assume that $\boldsymbol{H}_{\boldsymbol{k}}$ is paraunitarily equivalent to a diagonal matrix whose elements are all positive for any wave vector $\boldsymbol{k}$; all volume-mode bands obtained from original spin-wave Hamiltonian ($\lambda = 0$) are physically stable. Thanks to the Sylvester's law of inertia, such a Hermite matrix is unitarily equivalent to a diagonal matrix whose elements are all positive definite. Clearly, so is any $\boldsymbol{H}_{\boldsymbol{k},\lambda}$ during $0 \leqslant \lambda \leqslant 1$. Given the unitarily positive definiteness, we can then introduce from Eq. (4) a paraunitary matrix $\boldsymbol{T}_{\boldsymbol{k},\lambda}$ which transforms $\boldsymbol{H}_{\boldsymbol{k},\lambda}$ into a diagonal form as

$$\boldsymbol{H}_{\boldsymbol{k},\lambda}\boldsymbol{T}_{\boldsymbol{k},\lambda} = \boldsymbol{\sigma}_3\boldsymbol{T}_{\boldsymbol{k},\lambda}\begin{bmatrix}\boldsymbol{E}_{\boldsymbol{k},\lambda} & \\ & -\boldsymbol{E}_{-\boldsymbol{k},\lambda}\end{bmatrix},$$

with positive-definite N by N diagonal matrices $\boldsymbol{E}_{\boldsymbol{k},\lambda}$ and $\boldsymbol{E}_{-\boldsymbol{k},\lambda}$. With $\boldsymbol{T}_{\boldsymbol{k},\lambda}$, the Chern integer can be explicitly defined as a function of λ for $0 \leqslant \lambda \leqslant 1$, $C_j(\lambda)$.

The sum of the Chern integer over a group of bands does not change, unless some band in the group forms a band touching (frequency degeneracy) with bands outside the group. The positive definiteness of $\boldsymbol{E}_{\boldsymbol{k},\lambda}$ and $\boldsymbol{E}_{-\boldsymbol{k},\lambda}$ means that particle bands obtained from $\boldsymbol{H}_{\boldsymbol{k},\lambda}$ are always in the positive frequency regime, while hole bands are in the negative frequency regime; during the interpolation ($0 \leqslant \lambda \leqslant 1$), they are always disconnected from each other in frequency. Thus, the sum of the Chern integer over all particle bands does not change during the interpolation,

$$\sum_{j=1}^{N} C_j(\lambda = 0) = \sum_{j=1}^{N} C_j(\lambda = 1).$$

Since a paraunitary matrix at $\lambda = 1$ is trivial, $\boldsymbol{T}_{\boldsymbol{k},\lambda=1} = 1$, the right-hand side reduces to zero and so does the case with the original spin-wave Hamiltonian ($\lambda = 0$). In summary, Eq. (14) is derived only from the paraunitarily positive definiteness of $2N$ by $2N$ Hermite matrix $\boldsymbol{H}_{\boldsymbol{k}}$. As a corollary of Eq. (14), one can argue that any topological chiral edge modes obtained from proper spin-wave approximations appear only at a *finite* frequency region (see the Sec. IV for the argument). In the following, we show that a two-dimensional bicomponent magnonic crystal (MC) with the dipolar interaction supports spin-wave bands with nonzero Chern integers.

III. MAGNONIC CRYSTAL, DIPOLAR INTERACTION, AND CHERN INTEGER FOR VOLUME-MODE BANDS

A. Plane-wave theory for magnonic crystals

The MC considered is a ferromagnetic system with its magnetization and exchange interaction modulated periodically in the two-dimensional (x-y) direction. For simplicity, we assume that the system is translationally symmetric along the z direction, whereas the subsequent results are expected to be similar when a thickness of the system in the z direction becomes finite (but large). The system is composed of two kinds of ferromagnets: iron and YIG. The unit cell of the MC is an $a_x \times a_y$ rectangle, inside which iron is embedded into circular regions, while the remaining region is filled with YIG (Fig. 1). A uniform magnetic field H_0 is applied along the z direction, such that the static ferromagnetic moment M_s in both regions is fully polarized in the longitudinal direction. Propagation of the transverse moments (m_x,m_y) is described by a linearized Landau-Lifshitz equation,[27–30]

$$\frac{1}{|\gamma|\mu_0}\frac{dm_\pm}{dt} = \pm 2iM_s(\nabla\cdot Q\nabla)m_\pm \mp 2im_\pm(\nabla\cdot Q\nabla)M_s \\ \mp iH_0 m_\pm \pm ih_\pm M_s \tag{16}$$

with $\nabla \equiv (\partial_x,\partial_y)$, $m_\pm = m_x \pm im_y$, and $h_\pm = h_x \pm ih_y$. (h_x,h_y) stands for the transverse component of the long-ranged magnetic dipolar field $\boldsymbol{h}$, which is related to the ferromagnetic moment $\boldsymbol{m} \equiv (m_x,m_y,M_s)$ via the Maxwell equation, i.e., $\nabla\times\boldsymbol{h} = c^{-1}\partial_t e_z$ and $\nabla\cdot(\boldsymbol{h}+\boldsymbol{m}) = 0$. The former two terms in the right-hand side of Eq. (16) come from short-ranged exchange interaction, where Q denotes a square of the exchange interaction length. M_s and Q take values of iron inside the circular region and those of YIG otherwise. A filling fraction of the circular region with respect to the total area of the unit cell is represented by f. We further employ magnetostatic approximation, replacing the Maxwell equations by $\nabla \times \boldsymbol{h} = 0$ and $\nabla \cdot (\boldsymbol{h} + \boldsymbol{m}) = 0$;

$$h_\nu = -\partial_\nu \Psi, \quad \Delta\Psi = \partial_x m_x + \partial_y m_y, \tag{17}$$

with $\nu = x,y$. This in combination with Eq. (16) gives a closed equation of motion (EOM) for the transverse moment.

In order to obtain band dispersions and Chern integers for volume-mode bands, we need to reduce the EOM into a generalized eigenvalue problem with a BdG Hamiltonian ($\boldsymbol{H}_{\boldsymbol{k}}$) defined in the form of Eq. (1). To this end, we first normalize the transverse moment, to introduce a Holstein-Primakov (HP) field as[37]

$$\beta(\boldsymbol{r}) \equiv \frac{m_+(\boldsymbol{r})}{\sqrt{2M_s(\boldsymbol{r})}}, \quad \beta^\dagger(\boldsymbol{r}) \equiv \frac{m_-(\boldsymbol{r})}{\sqrt{2M_s(\boldsymbol{r})}}. \tag{18}$$

In terms of the HP field, the Landau-Lifshitz equation is properly symmetrized as

$$\begin{aligned}\frac{d\beta}{dt} &= 4i\alpha(\nabla\cdot Q\nabla)\alpha\beta - 4i\beta(\nabla\cdot Q\nabla)\alpha^2\\ &\quad - iH_0\beta - i\alpha\partial_+\Psi,\end{aligned} \tag{19}$$

$$\Delta\Psi = \partial_+(\alpha\beta^\dagger) + \partial_-(\alpha\beta), \quad \partial_\pm \equiv \partial_x \pm i\partial_y, \tag{20}$$

with $\alpha(\boldsymbol{r}) \equiv \sqrt{M_s(\boldsymbol{r})/2}$. $|\gamma|\mu_0$ was omitted in Eq. (19) for clarity. The static magnetization and exchange interaction are spatially modulated with the lattice periodicity;

$$\alpha(\boldsymbol{r}) = \sum_{\boldsymbol{G}} \alpha(\boldsymbol{G}) e^{i\boldsymbol{G}\cdot\boldsymbol{r}}, \quad Q(\boldsymbol{r}) = \sum_{\boldsymbol{G}} Q(\boldsymbol{G}) e^{i\boldsymbol{G}\cdot\boldsymbol{r}},$$

with the reciprocal vectors $\boldsymbol{G}$, $\alpha^*(\boldsymbol{G}) = \alpha(-\boldsymbol{G})$ and $Q^*(\boldsymbol{G}) = Q(-\boldsymbol{G})$. It follows from the Bloch theorem that $\boldsymbol{m}(\boldsymbol{r})$ and $\Psi(\boldsymbol{r})$ take a form

$$\begin{aligned}\beta(\boldsymbol{r}) &= \sum_{\boldsymbol{k}}\sum_{\boldsymbol{G}} \beta_{\boldsymbol{k}}(\boldsymbol{G}) e^{i(\boldsymbol{k}+\boldsymbol{G})\cdot\boldsymbol{r}},\\ \beta^\dagger(\boldsymbol{r}) &= \sum_{\boldsymbol{k}}\sum_{\boldsymbol{G}} \beta^\dagger_{\boldsymbol{k}}(\boldsymbol{G}) e^{-i(\boldsymbol{k}+\boldsymbol{G})\cdot\boldsymbol{r}},\end{aligned}$$

and

$$\Psi(\boldsymbol{r}) = \sum_{\boldsymbol{k}}\sum_{\boldsymbol{G}} \Psi_{\boldsymbol{k}}(\boldsymbol{G}) e^{i(\boldsymbol{k}+\boldsymbol{G})\cdot\boldsymbol{r}},$$

where the $\boldsymbol{k}$ summation is taken over the first BZ.

In terms of these Fourier modes, an equivalent generalized eigenvalue problem with a quadratic Hamiltonian for the HP field is derived as

$$i\frac{d}{dt}\begin{bmatrix}\boldsymbol{\beta}_{\boldsymbol{k}}\\ \boldsymbol{\beta}^\dagger_{-\boldsymbol{k}}\end{bmatrix} = \left[\begin{bmatrix}\boldsymbol{\beta}_{\boldsymbol{k}}\\ \boldsymbol{\beta}^\dagger_{-\boldsymbol{k}}\end{bmatrix}, \hat{\mathcal{H}}\right] = \boldsymbol{\sigma}_3 \boldsymbol{H}_{\boldsymbol{k}} \begin{bmatrix}\boldsymbol{\beta}_{\boldsymbol{k}}\\ \boldsymbol{\beta}^\dagger_{-\boldsymbol{k}}\end{bmatrix}, \tag{21}$$

with

$$\hat{\mathcal{H}} = \sum_{k_y>0} [\boldsymbol{\beta}^\dagger_{\boldsymbol{k}}\ \boldsymbol{\beta}_{-\boldsymbol{k}}] \boldsymbol{H}_{\boldsymbol{k}} \begin{bmatrix}\boldsymbol{\beta}_{\boldsymbol{k}}\\ \boldsymbol{\beta}^\dagger_{-\boldsymbol{k}}\end{bmatrix},$$

and

$$\begin{aligned}\begin{bmatrix}\boldsymbol{\beta}_{\boldsymbol{k}}\\ \boldsymbol{\beta}^\dagger_{-\boldsymbol{k}}\end{bmatrix} &\equiv [\ldots,\beta_{\boldsymbol{k}}(\boldsymbol{G}),\ldots,\beta_{\boldsymbol{k}}(-\boldsymbol{G}),\ldots,|\\ &\qquad \ldots,\beta^\dagger_{-\boldsymbol{k}}(-\boldsymbol{G}),\ldots\beta^\dagger_{-\boldsymbol{k}}(\boldsymbol{G}),\ldots]^T,\\ [\boldsymbol{\beta}^\dagger_{\boldsymbol{k}}\ \boldsymbol{\beta}_{-\boldsymbol{k}}] &\equiv [\ldots,\beta^\dagger_{\boldsymbol{k}}(\boldsymbol{G}),\ldots\beta^\dagger_{\boldsymbol{k}}(-\boldsymbol{G}),\ldots,|\\ &\qquad \ldots,\beta_{-\boldsymbol{k}}(-\boldsymbol{G}),\ldots\beta_{-\boldsymbol{k}}(\boldsymbol{G}),\ldots].\end{aligned}$$

$\boldsymbol{\sigma}_3$ in the right-hand side takes ± 1 in the particle/hole space, which comes from the commutation relation of bosons, $[\boldsymbol{\beta}_{\boldsymbol{k}},\boldsymbol{\beta}^\dagger_{\boldsymbol{k}}] = \boldsymbol{1}$ and $[\boldsymbol{\beta}^\dagger_{-\boldsymbol{k}},\boldsymbol{\beta}_{-\boldsymbol{k}}] = -\boldsymbol{1}$. A comparison between Eqs. (19) and (20) and Eq. (21) dictates that $\boldsymbol{H}_{\boldsymbol{k}}$ thus introduced is given by the following Hermitian matrix ($\boldsymbol{H}^\dagger_{\boldsymbol{k}} = \boldsymbol{H}_{\boldsymbol{k}}$):

$$\boldsymbol{H}_{\boldsymbol{k}} \equiv \begin{bmatrix}\boldsymbol{\alpha}\cdot\boldsymbol{\alpha} + \boldsymbol{B}_{\boldsymbol{k}} + H_0\boldsymbol{1} & \boldsymbol{\alpha}\cdot\boldsymbol{I}_{\boldsymbol{k}}\cdot\boldsymbol{\alpha}\\ \boldsymbol{\alpha}\cdot\boldsymbol{I}^*_{\boldsymbol{k}}\cdot\boldsymbol{\alpha} & \boldsymbol{\alpha}\cdot\boldsymbol{\alpha} + \boldsymbol{B}_{\boldsymbol{k}} + H_0\boldsymbol{1}\end{bmatrix} \tag{22}$$

with

$$\begin{aligned}&[\boldsymbol{\alpha}]_{\boldsymbol{G},\boldsymbol{G}'} \equiv \alpha(\boldsymbol{G}-\boldsymbol{G}'),\ [\boldsymbol{I}_{\boldsymbol{k}}]_{\boldsymbol{G},\boldsymbol{G}'} \equiv \delta_{\boldsymbol{G},\boldsymbol{G}'} e^{-2i\theta_{\boldsymbol{k}}(\boldsymbol{G})},\\ &e^{i\theta_{\boldsymbol{k}}(\boldsymbol{G})} \equiv \frac{(\boldsymbol{k}+\boldsymbol{G})_x + i(\boldsymbol{k}+\boldsymbol{G})_y}{|\boldsymbol{k}+\boldsymbol{G}|},\end{aligned} \tag{23}$$

and

$$\begin{aligned}[\boldsymbol{B}_{\boldsymbol{k}}]_{\boldsymbol{G},\boldsymbol{G}'} \equiv\ & 4\sum_{\boldsymbol{G}_1,\boldsymbol{G}_2} \alpha(\boldsymbol{G}-\boldsymbol{G}_1)Q(\boldsymbol{G}_1-\boldsymbol{G}_2)\alpha(\boldsymbol{G}_2-\boldsymbol{G}')\\ &\times(\boldsymbol{k}+\boldsymbol{G}_1)\cdot(\boldsymbol{k}+\boldsymbol{G}_2)\\ &-4\sum_{\boldsymbol{G}_1,\boldsymbol{G}_2} Q(\boldsymbol{G}_1)\alpha(\boldsymbol{G}_2)\alpha(\boldsymbol{G}-\boldsymbol{G}'-\boldsymbol{G}_1-\boldsymbol{G}_2)\\ &\times(\boldsymbol{G}-\boldsymbol{G}')\cdot(\boldsymbol{G}-\boldsymbol{G}'-\boldsymbol{G}_1).\end{aligned} \tag{24}$$

After taking the summation over $\boldsymbol{G}_1$ and $\boldsymbol{G}_2$ in Eq. (24), one can further decompose $[\boldsymbol{B}_{\boldsymbol{k}}]_{\boldsymbol{G},\boldsymbol{G}'}$ into three parts,

$$\begin{aligned}[\boldsymbol{B}_{\boldsymbol{k}}]_{\boldsymbol{G},\boldsymbol{G}'} =\ & 4\sum_{\mu=x,y}[Q\alpha^2]_{\boldsymbol{G}-\boldsymbol{G}'}(\boldsymbol{k}+\boldsymbol{G})_\mu(\boldsymbol{k}+\boldsymbol{G}')_\mu\\ &+4i\sum_{\mu=x,y}[Q\alpha(\partial_\mu\alpha)]_{\boldsymbol{G}-\boldsymbol{G}'}(\boldsymbol{G}-\boldsymbol{G}')_\mu\\ &+4\sum_{\mu=x,y}[Q(\partial_\mu\alpha)(\partial_\mu\alpha)]_{\boldsymbol{G}-\boldsymbol{G}'}\end{aligned} \tag{25}$$

with

$$\begin{aligned}[Q\alpha^2]_{\boldsymbol{G}} &\equiv \frac{1}{S}\int Q(\boldsymbol{r})\alpha^2(\boldsymbol{r})e^{-i\boldsymbol{G}\cdot\boldsymbol{r}}d^2\boldsymbol{r},\\ [Q\alpha(\partial_\mu\alpha)]_{\boldsymbol{G}} &\equiv \frac{1}{S}\int Q(\boldsymbol{r})\alpha(\boldsymbol{r})[\partial_\mu\alpha(\boldsymbol{r})]e^{-i\boldsymbol{G}\cdot\boldsymbol{r}}d^2\boldsymbol{r},\\ [Q(\partial_\mu\alpha)(\partial_\mu\alpha)]_{\boldsymbol{G}} &\equiv \frac{1}{S}\int Q(\boldsymbol{r})[\partial_\mu\alpha(\boldsymbol{r})][\partial_\mu\alpha(\boldsymbol{r})]e^{-i\boldsymbol{G}\cdot\boldsymbol{r}}d^2\boldsymbol{r},\end{aligned} \tag{26}$$

where the two-dimensional (2D) integrals in the right-hand side are taken over the MC unit cell and S denotes an area of the cell ($S \equiv a_x a_y$). In actual numerical calculation, the dimension of $\boldsymbol{H}_{\boldsymbol{k}}$ is typically taken to be 512×512, where the reciprocal-vector $\boldsymbol{G}$ ranges over $[-16\pi/a_x, 16\pi/a_x] \times [-16\pi/a_y, 16\pi/a_y]$.

The MC considered is composed of two kinds of ferromagnets, where the respective (square root of) magnetization and (square of) exchange interaction length are specified by

(α_j,Q_j) $(j=1,2)$. Within the rectangular-shaped unit cell $(a_x\times a_y)$, one of these two ferromagnets (α_1,Q_1) is embedded within the circular region, while the remaining region is filled with the other (α_2,Q_2). If $\alpha(\boldsymbol{r})$ has a discontinuity at the boundary between these two regions, the last term in Eq. (25), $[Q(\partial_\mu\alpha)(\partial_\mu\alpha)]$, diverges, since it contains the second derivative with respect to a spatial coordinate along the radial direction. Physically, such an infrared divergence is removed by a smooth variation of the saturation magnetization at the boundary. For simplicity, we interpolate $\alpha(\boldsymbol{r})$ as a linear function of the radial coordinate measured from the center of the circular region,

$$\alpha(\boldsymbol{r})=\begin{cases}\alpha_1 & (|\boldsymbol{r}|<R_0),\\ \alpha_1-\frac{|\boldsymbol{r}|-R_0}{R_1-R_0}(\alpha_1-\alpha_2) & (R_0<|\boldsymbol{r}|<R_1),\\ \alpha_2 & (R_1<|\boldsymbol{r}|).\end{cases}\quad (27)$$

A discontinuity in $Q(\boldsymbol{r})$ is also removed by the same linear interpolation. Actual numerics are carried out with $(r_0,r_1)\equiv(R_0/\lambda,R_1/\lambda)=(0.10,0.125)$, where λ denotes the linear dimension of the unit-cell size, $\lambda\equiv\sqrt{a_xa_y}$. As for the material parameter, we used $(M_{s,1},M_{s,2})=(1.8,0.19)(\mathrm{A}/\mu\mathrm{m})$ and $(\sqrt{Q_1},\sqrt{Q_2})=(33,130)$ (Å) with $\alpha_j\equiv\sqrt{M_{s,j}}$, while parameters of iron (Fe), cobalt (Co), and YIG are $[M_s\ (\mathrm{A}/\mu\mathrm{m}),\sqrt{Q}\ (\text{Å})]=(1.7,21),(1.4,29)$, and $(0.14,184)$, respectively.

Under $\boldsymbol{T_k}$, the EOM is paraunitarily equivalent to

$$i\frac{d}{dt}\begin{bmatrix}\boldsymbol{\gamma_k}\\ \boldsymbol{\gamma}^\dagger_{-\boldsymbol{k}}\end{bmatrix}=\begin{bmatrix}\boldsymbol{E_k} & \\ & -\boldsymbol{E}_{-\boldsymbol{k}}\end{bmatrix}\begin{bmatrix}\boldsymbol{\gamma_k}\\ \boldsymbol{\gamma}^\dagger_{-\boldsymbol{k}}\end{bmatrix}.$$

$[\boldsymbol{E_k}]_j$ gives a dispersion relation for the jth volume-mode band $(j=1,\ldots)$, while the Chern integer is calculated from $\boldsymbol{T_k}$ via Eqs. (8)–(10). In its numerical evaluation, we employed an algorithm based on a "manifestly gauge-invariant" description of the Chern integer.[38]

B. Role of dipolar interaction

When a system considered is either time-reversal symmetric; $\boldsymbol{H}^*_{-\boldsymbol{k}}=\boldsymbol{H_k}$, or mirror-symmetric with a mirror plane perpendicular to the xy plane, e.g., $\boldsymbol{H}_{(k_x,k_y)}=\boldsymbol{H}_{(k_x,-k_y)}$, the Berry's curvature satisfies $-B_j(\boldsymbol{k})=B_j(-\boldsymbol{k})$ or $-B_j(k_x,k_y)=B_j(k_x,-k_y)$, respectively, which reduces the Chern integer to zero. In the present situation, however, the magnetic dipolar field brings about complex-valued phase factors in the anomalous part, $\boldsymbol{I_k}\neq\boldsymbol{I}^*_{\boldsymbol{k}}$, which removes from Eq. (22) both the time-reversal symmetry and the mirror symmetries. Without periodic modulation of the saturation magnetization, $\boldsymbol{\alpha}=\alpha\boldsymbol{1}$, these phase factors can be erased by a proper gauge transformation, $\boldsymbol{\beta}^\dagger_{\boldsymbol{k}}\rightarrow\boldsymbol{\beta}^\dagger_{\boldsymbol{k}}\sqrt{\boldsymbol{I}^*_{\boldsymbol{k}}}$ and $\boldsymbol{\beta}_{-\boldsymbol{k}}\rightarrow\boldsymbol{\beta}_{-\boldsymbol{k}}\sqrt{\boldsymbol{I_k}}$, so that both symmetries are recovered. In the presence of the periodic modulations, $\boldsymbol{\alpha}\neq\alpha\boldsymbol{1}$, however, these two symmetries are generally absent in the 2D MCs and the bosonic Chern integer can take a nonzero integer value.

This situation is quite analogous to what the relativistic spin-orbit interaction does in ferromagnetic metals.[39,40] Moreover, contrary to the spin-orbit interaction, a strength of the dipolar interaction is an experimentally tunable parameter in MCs.[22] When characteristic length scale of MC (linear dimension of the unit-cell size $\lambda\equiv\sqrt{a_xa_y}$) becomes larger than the typical exchange length $\sqrt{Q}$, the dipolar interaction is expected to prevail over the exchange interaction.

C. Chern integer of volume-mode bands and role of band touchings

In fact, we found that the Chern integer of the lowest magnonic band, C_1, is always quantized to be 2 for the longer λ, while the integer reduces to zero for the shorter λ [Fig. 2(a)]. The respective quantization is protected by a finite direct band gap between the lowest band and the second lowest band [Fig. 2(b)]. In the intermediate regime of λ, these two bands get closer to each other. With a fourfold rotational symmetry $(r\equiv a_y/a_x=1)$, the gap closes at the two X points at a critical value of λ ($\sim$0.28 μm), where the two bands form gapless Dirac spectra [Fig. 2(c)]. Without the fourfold symmetry $(r\neq1)$, the band touching at one of the two X points and that of the other occur at different values of λ. These band touchings are denoted as $P_1(\pi,0,\lambda_{c,1})$ and $P_2(0,\pi,\lambda_{c,2})$ in

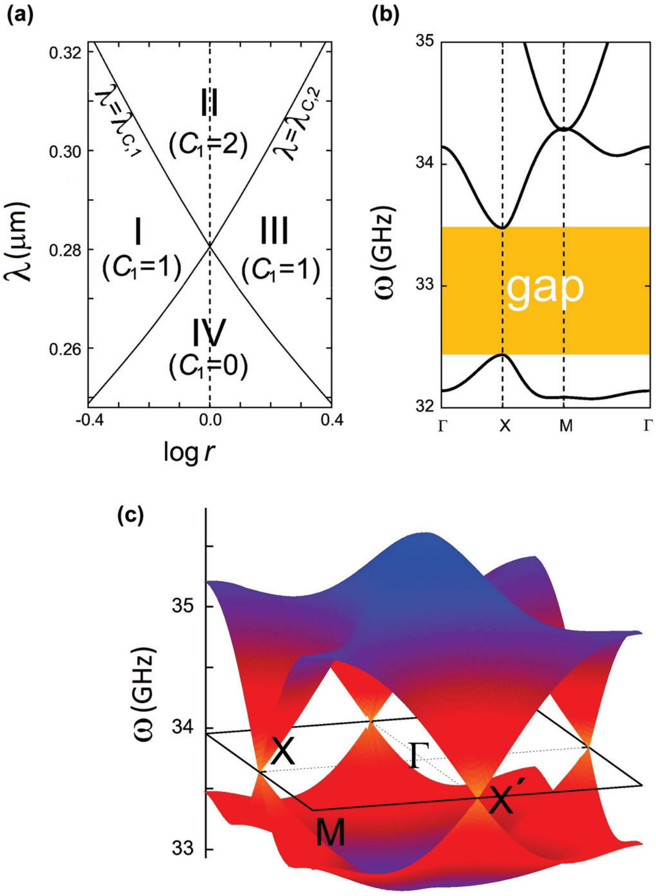

FIG. 2. (Color online) Chern-integer phase diagram and band dispersions with $f=\pi\times10^{-2}$. (a) Chern-integer phase diagram. The phases are distinguished by the Chern integer of the lowest magnonic band, C_1. r stands for the aspect ratio of the unit-cell shape $(r\equiv a_y/a_x)$. (b) Band dispersions of the lowest three volume-mode bands with $r=1$, and $\lambda=0.35$ μm. A band gap appears between the first and the second lowest band. (c) The band gap collapses at $\lambda=0.28$ μm $(r=1)$, where the lowest and second lowest volume mode form Dirac cones at the two inequivalent X points.

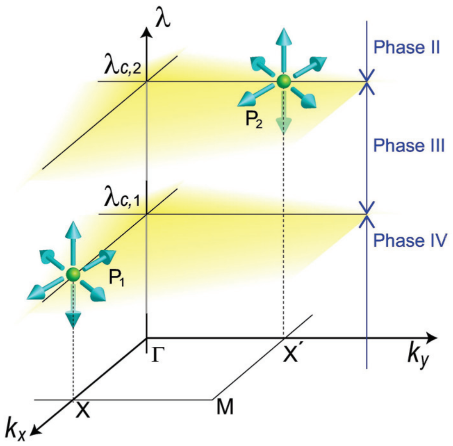

FIG. 3. (Color online) Band-touching points (dual magnetic charges) in a three-dimensional parameter space subtended by the wave vector (k_x, k_y) and the unit-cell size ($\lambda \equiv \sqrt{a_x a_y}$) for $r > 1$. Small green spheres denote the band-touching points, which emit the dual magnetic field (blue arrows).

a three-dimensional parameter space subtended by two wave vectors k_x, k_y and the unit-cell size λ (Fig. 3).

The band touchings endow the lowest volume-mode band with nonzero Chern integers in the longer λ region. In generalized eigenvalue problems as well as usual eigenvalue problems,[35,36,41,42] a band-touching point in the 3D parameter space plays role of a dual magnetic monopole (charge). The corresponding dual magnetic field is generalized from Eq. (8) as a rotation of the three-component gauge field $\boldsymbol{A}_j = (A_{j,x}, A_{j,y}, A_{j,\lambda})$,

$$\boldsymbol{B}_j = \nabla \times \boldsymbol{A}_j \tag{28}$$

with $\nabla \equiv (\partial_{k_x}, \partial_{k_y}, \partial_\lambda)$. Here the third component of the gauge field $A_{j,\lambda}$ is introduced in the same way as in (9):

$$A_{j,\lambda} \equiv i\mathrm{Tr}[\boldsymbol{\Gamma}_j \boldsymbol{\sigma}_3 \boldsymbol{T}_{\boldsymbol{k}}^\dagger \boldsymbol{\sigma}_3 (\partial_\lambda \boldsymbol{T}_{\boldsymbol{k}})]. \tag{29}$$

j specifies either one of the two magnonic bands which form the band touching. At the band-touching point, the dual magnetic field for the respective bands has a dual magnetic charge, whose strength is quantized to be 2π times integer (see the Appendix). A numerical evaluation tells us that the dual magnetic charges for the lowest band at the band-touching points at P_1 and P_2 are both $+2\pi$ (Fig. 3),

$$\begin{aligned}\nabla \cdot \boldsymbol{B}_1 = {} & 2\pi\delta(\lambda - \lambda_{c,1})\delta(k_x - \pi)\delta(k_y) \\ & + 2\pi\delta(\lambda - \lambda_{c,2})\delta(k_x)\delta(k_y - \pi),\end{aligned}$$

where $\lambda_{c,1} < \lambda_{c,2}$ for $a_y > a_x$ $(r > 1)$ and $\lambda_{c,1} > \lambda_{c,2}$ for $a_y < a_x$ $(r < 1)$.

Because the Chern integer can be regarded as the total dual magnetic flux penetrating through the constant λ plane [see Eq. (10)], the Gauss theorem suggests that, when λ goes across either the $\lambda = \lambda_{c,1}$ plane or the $\lambda = \lambda_{c,2}$ plane, the Chern integer for the lowest magnonic band always changes by unit, e.g.,

$$C_1|_{\lambda > \lambda_{c,1}} - C_1|_{\lambda_{c,1} > \lambda} = 1.$$

Without the fourfold rotational symmetry ($r \neq 1$), the two critical values of λ bound three phases for the lowest magnonic band, the phase with $C_1 = 0$ (phase IV), that with $C_1 = 1$ (phase III or I), and that with $C_1 = 2$ (phase II). In the presence of the fourfold rotational symmetry ($r = 1$), two band touchings occur at the same critical value of λ, where C_1 increases by 2 on increasing λ. This leads to a phase diagram shown in Fig. 2(a), which describes the Chern integer of the lowest magnonic band as a function of the unit-cell size λ and the aspect ratio r.

A dual magnetic charge is a quantized topological object, so that, upon any small change of parameters, it cannot disappear by itself. Instead, it only moves around in the 3D parameter space. As a result, the global structure of the phase diagram depicted in Fig. 2(a) widely holds true for other combinations of material parameters. For $r = 1$ and $f = \pi \times 10^{-2}$, we found $\lambda_c = 0.370\ \mu$m for iron (circular region) and YIG (host), and $\lambda_c = 0.372\ \mu$m for cobalt (circular region) and YIG (host). When varying the filling fraction for iron (circular region) and YIG (host) with $r = 1$, we found $\lambda_c = 0.274\ \mu$m for $f = 4\pi \times 10^{-2}$, and $\lambda_c = 0.348\ \mu$m for $f = 9\pi \times 10^{-2}$.

IV. CHIRAL SPIN-WAVE EDGE MODE IN MC

The chiral phases with nonzero Chern integers have chiral spin-wave edge modes, which are localized at a boundary with the phase with zero Chern integer (phase IV) or the vacuum. The edge modes have chiral dispersions which go across the band gap between the lowest and the second lowest band.

As an illustrative example, we consider a boundary (y axis) between the MC in phase III ($C_1 = 1$) and the MC in the phase IV ($C_1 = 0$). The existence of a chiral spin-wave edge mode at the boundary is shown from a following 2×2 Dirac Hamiltonian derived near their phase boundary $\lambda = \lambda_{c,1}$ (see the Appendix),

$$\mathcal{H}_{\text{eff}} = \omega_0 \boldsymbol{\tau}_0 + \kappa(x)\boldsymbol{\tau}_3 - ia\partial_x \boldsymbol{\tau}_1 - ib\partial_y \boldsymbol{\tau}_2. \tag{30}$$

$\boldsymbol{\tau}_j$ denotes the Pauli matrices subtended by the twofold degenerate eigenstates at P_1. a and b are positive material parameters. The difference of the Chern integers (C_1) for the two phases is represented as a change of sign of a Dirac mass term $\kappa(x)$: $\kappa(x) > 0$ for $x > 0$ (phase III) and and $\kappa(x) < 0$ for $x < 0$ (phase IV) [see Fig. 4(a)]; $\lim_{x \to \pm\infty} \kappa(x) = \pm\kappa_\infty$. The Hamiltonian has a following eigenstate:[43,44] $\boldsymbol{\psi}_k(\boldsymbol{r}) \propto e^{iky} e^{-(1/a)\int^x \kappa(x')dx'} [1, i]^t$, which is localized at the boundary ($x = 0$). In terms of the surface wave vector k along the y axis, the corresponding eigenfrequency is given by $E = \omega_0 + bk$. This connects the lowest magnonic band lying at $E \leqslant \omega_0 - \kappa_\infty$ and the second lowest band at $E \geqslant \omega_0 + \kappa_\infty$ [see Figs. 4(b) and 4(c)]. The mode is chiral, since the group velocity is always positive, $v_k \equiv \partial_k E = b$. Similarly, we can easily show that the phase with $C_1 = 1$ at $r > 1$ (phase III) or $r < 1$ (phase I) has a chiral edge mode at its boundary with vacuum, whose dispersion crosses the direct band gap at the $(\pi, 0)$ or $(0, \pi)$ point, respectively, while the phase with $C_1 = 2$ (phase II) has both at its boundary with vacuum. A number of chiral modes localized at the interface between two MCs with different Chern integers is equal to the difference of the two Chern integers.

Generalizing the arguments so far into the linearly interpolated Hamiltonian defined in Eq. (15), we can argue that, in general, a number of those chiral spin-wave edge modes

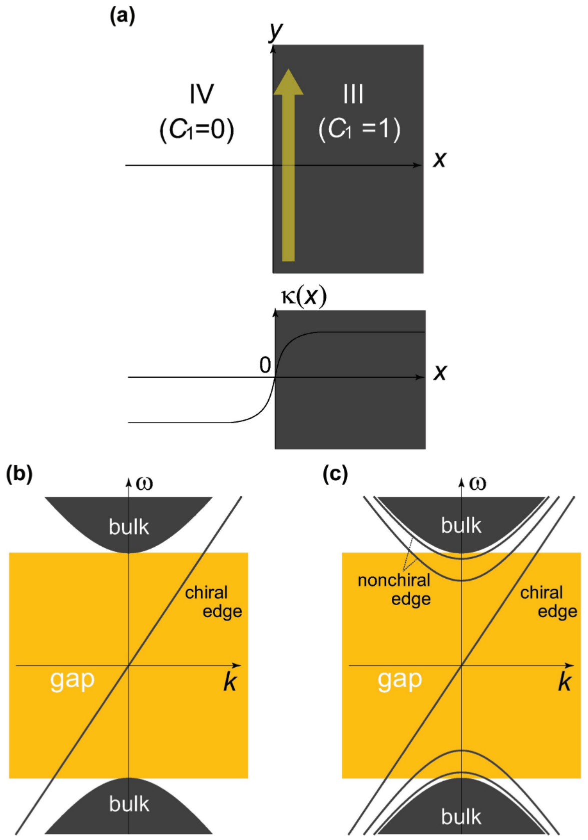

FIG. 4. (Color online) Chiral spin-wave edge modes. (a) Geometry of the system. (b),(c) Wave-vector frequency dispersions for Dirac Hamiltonian with the Pöschl-Teller potential (Ref. 15) $\kappa(x) = \kappa_\infty \tanh(x/d)$ for $\kappa_\infty d = 0.9a$ (b), and $\kappa_\infty d = 2.9a$ (c). The volume-mode magnonic bands have a band gap, inside which an edge mode has a chiral dispersion. In (c) there are some nonchiral edge states, whereas in (b) there is not. Nonetheless, the number of chiral edge modes is one, which is determined solely from the difference between the Chern integers for the two phases.

whose dispersions run across a gap between the mth and the $(m+1)$th particle bands, N_m, is equal to the sum of the Chern integer over those *particle* bands below the gap,

$$N_m \equiv \sum_{j=1}^{m} C_j. \qquad (31)$$

Here clockwise (counterclockwise) chiral edge modes contribute by $+1$ (-1) to the number of chiral edge modes, N_m [see Fig. 4(a)]. Namely, the sum rule, Eq. (14), suggests that the right-hand side of Eq. (31) counts the total number of the band touchings (including the sign of the respective dual magnetic charges) which happen between the mth particle band and $(m+1)$th particle band during the interpolation, $\lambda = 1 \to \lambda = 0$. On the one end, each band touching (dual magnetic monopole) is accompanied by the emergence of a chiral edge mode between these two bands, whose sense of rotation is either clockwise or counterclockwise, depending on the sign of the respective dual magnetic charge. Since there are no chiral edge modes in the trivial limit $(\lambda = 1)$, we can safely conclude Eq. (31) at $\lambda = 0$. As a corollary of Eq. (31), one can also see that any topological chiral edge modes obtained from legitimate spin-wave approximation appear only at a finite frequency region, never a gapless mode.

Chiral edge modes proposed in this paper share similar physical properties with the well-known Damon-Eshbach (DE) surface mode,[19] instead of backward volume modes studied so far in actual magnonic cyrstals.[45–48] The topological modes as well as the DE surface mode are propagating in a chiral way along boundaries (surfaces) of the systems, where the propagation directions are parallel (or antiparallel) to vector products between the polarized ferromagnetic moment and the normal vectors associated with surfaces. Experimental techniques for measuring the DE surface mode can be also utilized for detecting the proposed topological chiral edge modes. Possible experiments include Brillouin light-scattering (BLS) measurements,[49–51] time-resolved Kerr microscopy,[52] infrared thermography,[53] and scanning local magnetic fields in terms of a wire loop or antenna.[54]

The topological edge mode always has a chiral dispersion within a band gap for volume-mode bands. When a radio frequency (rf) of applied microwave is chosen inside the band gap, spin waves are excited only along these chiral edge modes, while other volume modes remain intact. One can test this situation by changing the position of an input antenna from the boundaries to an interior far from the boundaries. Being protected by the topological Chern integers defined for volume modes, the proposed chiral edge modes are expected to be robust against various perturbations introduced near the boundaries. The robustness can be also tested by changing boundary shape or introducing boundary roughness and obstacle.

Contrary to the DE mode, Eq. (31) dictates that the number and the sense of rotation of the topological chiral edge modes are determined by the Chern integer for volume modes below the band gap. In fact, the chiral edge mode in the proposed magnonic crystal rotates along the boundary in the *clockwise* manner with an up-headed magnetic field (Fig. 1), while the DE surface mode with the same geometry rotates in the *counterclockwise* way with the up-headed field.[18,19] Moreover, the Chern integer for a volume-mode band itself can be changed by closing the band gap, as was shown in the previous section. Thus, using band-gap manipulation, one can even control the chiral direction[55] or the number of the mode, which enable intriguing spintronic devices such as a spin-current splitter (see also Sec. VI). To our best knowledge, the DE mode in a uniform thin film does not have such properties.

V. MICROMAGNETIC SIMULATION FOR CHIRAL TOPOLOGICAL EDGE MODES

A. Simulation procedure and material parameters

To justify the existence of topological chiral spin-wave edge modes in the present MC model, we have numerically simulated the Landau-Lifshitz-Gilbert equation,

$$\frac{d\boldsymbol{m}}{dt} = -\gamma|\mu_0|\boldsymbol{m} \times \mathbf{H}_{\text{eff}} + \frac{\overline{\alpha}}{M_s}\boldsymbol{m} \times \frac{d\boldsymbol{m}}{dt}, \qquad (32)$$

where $\overline{\alpha}$ is set to the Gilbert damping coefficient of YIG; $\overline{\alpha} = 6.7 \times 10^{-5}$.[56] The magnetic field $\mathbf{H}_{\text{eff}}$ includes a short-ranged exchange field, a long-ranged dipolar field $\boldsymbol{h}$, the static longitudinal external field $H_0 = 0.1$ T, and a small temporally alternating transverse field ($H_1 \boldsymbol{e}_x \cos \omega t$) with $H_1 = 1.0$ Oe. A simulated magnonic crystal (MC) is as large as either 28 μm $\times$ 28 μm or 7 μm $\times$ 7 μm in the x-y plane, which is composed of 80 $\times$ 80 or 20 $\times$ 20 MC unit cells, respectively; each unit-cell size is 350 nm $\times$ 350 nm within the plane. A MC unit cell consists of an YIG region and a Fe region, where the size of the Fe region is 140 nm $\times$ 140 nm ($f = 0.16$). The MC studied in the previous sections is translationally symmetric along the z direction. To mimic this situation in a micromagnetic simulation, we take the thickness along the z direction L_z to be sufficiently large ($L_z = 1$ mm).

In actual simulation, each MC unit cell is further discretized into a bunch of smaller elements,[57] each of which is taken in this study as large as 70 nm $\times$ 70 nm $\times$ L_z and each element is assigned with one ferromagnetic spin, which is uniformly distributed over the element. Namely, every MC unit cell has 25 spins consisting of 4 Fe spins and 21 YIG spins. The short-ranged exchange stiffness between Fe elements is taken to be $A_{\mathrm{Fe}} = 2.1 \times 10^{-11}$ J/m, between YIG elements $A_{\mathrm{YIG}} = 0.437 \times 10^{-11}$ J/m, and between Fe and YIG elements $A_{\mathrm{Fe-YIG}} = 1.0 \times 10^{-11}$ J/m. These set material parameters to be those in the dipolar regime with $C_1 = 2$ ($H_0 = 0.1$T, $\lambda = 0.35\mu$m, $r = 1$, and $f = 0.16$).

The superelongated cell size (70 nm $\times$ 70 nm $\times$ L_z with $L_z = 1$ mm) used in this simulation clearly ignores those spin-wave modes which have *nodes* along the z direction. In the presence of very large thickness along the z direction (e.g., 28 μm $\times$28 μm $\times$ 1 mm), however, it is likely that the strong magnetic shape anisotropy pushes up such spin-wave modes into higher frequency regimes; spin-wave excitations in lower-frequency regime, which we focus on in the present study, are mainly dominated by those modes having *no* node along the z direction. Even for spin-wave modes without nodes along the z direction, their wave functions should be certainly modified near the boundaries along the direction. When the thickness along the direction is much larger than the linear dimension within the other two directions (xy plane), however, the modifications of the wave functions are also expected to be small.

The time evolution is determined by Eq. (32), which is numerically integrated with a time interval of 1 ps by use of the fourth-order Runge-Kutta method. The demagnetization field $\boldsymbol{h}$ is calculated by the convolution of a kernel which describes the dipole-dipole interaction. With the Gilbert damping term, the system eventually reaches a certain steady state, in which only the spin-wave modes around the external frequency ω are excited permanently. In order to deduce spatial distribution of spin-wave modes at a given frequency, we have studied steady states ($\omega t \gg 1$) with changing the external frequency.

To compare simulation results with dispersions for the volume-mode bands obtained from the plane-wave theory, we also take a Fourier transformation of transverse moments over space and time in a steady state. Specifically, we perform a discrete Fourier transformation of $m_+ \equiv m_x + i m_y$ with respect to space and time coordinate as

$$m_+(k_x,k_y.\omega) \equiv \sum_{X,Y} \sum_j m_+(X,Y,j\Delta T) e^{ik_x X + ik_y Y - i\omega j \Delta T}.$$

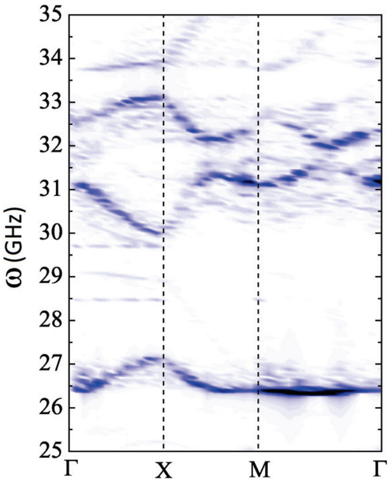

FIG. 5. (Color online) A contour plot of $|m_+(k_x,k_y,\omega)|$ as a function of k_x, k_y, and ω, which has stronger amplitude in blue-colored regions and smaller amplitude in white regions. The contour plot signifies dispersion relations for volume-mode bands [compare with Fig. 2(b)]. The wave vector (k_x,k_y) is along (0,0) (Γ point), (π,0) (X point), (π,π) (M point), and (0,0) (Γ point). In this calculation, the system size is taken to be 7 μm$\times$ 7 μm. In this system size, we observe chiral edge modes similar to those in Figs. 6(c)–6(f) within 27 GHz$< \omega <$30 GHz.

A contour plot of (absolute value of) the left-hand side as a function of k_x, k_y, and ω is expected to give dispersion relations for spin-wave volume-mode bands.

B. Result

Throughout the micromagnetic simulation, we found that a lower frequency region can be roughly classified into three characteristic regimes: two volume-mode frequency regimes, (i) $\omega_0 < \omega < \omega_1$ and (iii) $\omega_2 < \omega$, and a band-gap regime for volume modes, (ii) $\omega_1 < \omega < \omega_2$. Below ω_0, the system remains intact against the small alternating transverse field, indicating no spin-wave modes for $\omega < \omega_0$. Within the volume-mode frequency regimes (i) $\omega_0 < \omega < \omega_1$ [Fig. 6(a)] and (iii) $\omega_2 < \omega$ [Fig. 6(b)], spin-wave excitations in steady states are always distributed over the entire system. A comparison between Fig. 2(b) and the contour plot of the Fourier transform of the transverse moments (Fig. 5) indicates that these two frequency regimes correspond to the lowest volume-mode band and higher volume-mode bands, respectively.

On the one hand, a steady state in the intermediate frequency regime, $\omega_1 < \omega < \omega_2$, has almost no weight for volume modes. Instead, spin-wave excitations in the intermediate regime are localized only around the boundaries of the system [see Fig. 6(c)], indicating the existence of spin-wave edge modes. Moreover, these edge modes propagate in a *chiral* way [see Figs. 6(d)–6(f)], whose direction is consistent with a chiral direction determined from the Chern integer in the dipolar regime found in Fig. 2(a), $C_1 = +2 > 0$. These observations indicate that the spin-wave edge modes found in the intermediate frequency region is nothing but the topological chiral spin-wave edge modes described in the previous section. In fact, the three frequency regimes are qualitatively consistent with the plane-wave-theory

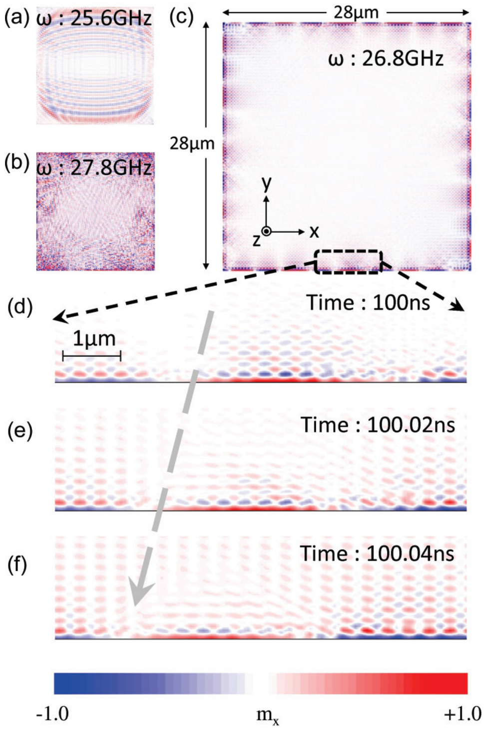

FIG. 6. (Color online) Snapshots of spatial distribution of spin-wave excitations in steady states. In this calculation, the system size is taken to be 28 μm× 28 μm. A normalized transverse component of the ferromagnetic spin, $m_x \equiv n_x/n_{\max}$, is plotted, where $n_{\max}$ denotes the maximum value of $\sqrt{n_x^2+n_y^2}$ with $(n_x,n_y,n_z) \equiv m/M_s$. The static magnetic field is taken along the $+z$ direction. (a) Snapshot of m_x at $t = 100$ ns with the external frequency $\omega_0 < \omega < \omega_1$ ($\omega = 25.6$ GHz). (b) Snapshot at $t = 100$ ns with $\omega_2 < \omega$ ($\omega = 27.8$ GHz). (c) Snapshot at $t = 100$ ns with $\omega_1 < \omega < \omega_2$ ($\omega = 26.8$ GHz). (d)–(f) Spin-wave edge modes at $\omega = 26.8$ GHz are propagating in a chiral way. (d) $t = 100$ ns, (e) $t = 100.02$ ns, (f) $t = 100.04$ ns.

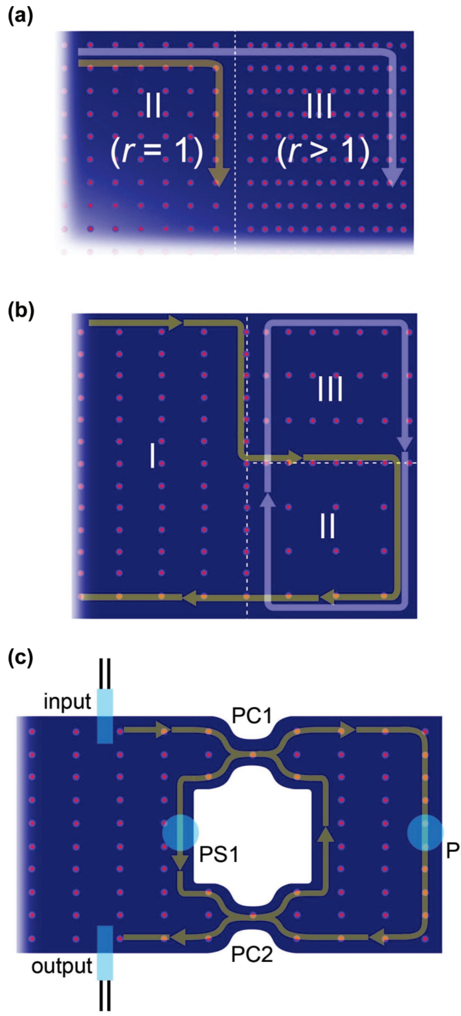

FIG. 7. (Color online) Examples of magnonic circuit made by chiral magnonic edge modes. (a),(b) Schematic pictures of spin-current splitter. (c) Magnonic analog of the Fabry-Perot interferometer.

calculation [Fig. 2(b)]; $(\omega_0,\omega_1,\omega_2) = (25.5, 26.0{,}27.5$ GHz) for 28 μm × 28 μm × 1 mm, and (26.2, 27.1, 30.0 GHz) for 7 μm × 7 μm × 1 mm. Our micromagnetic simulation with a shorter sample thickness ($L_z = 200$ μm) also justifies the existence of topological chiral modes.

VI. DISCUSSION

By calculating a newly introduced bosonic Chern integer for spin-wave bands, we argue that a two-dimensional normally magnetized magnonic crystal acquires chiral edge modes for magnetostatic wave in the dipolar regime. Each mode is localized at the boundary of the system, carrying magnetic energies in a unidirectional way. Thanks to the topological protection, spin-wave propagations along these edge modes are robust against imperfections of the lattice periodicity and boundary roughness; they are free from any types of elastic backward scatterings with moderate strength.[58] This robustness makes it possible to implement novel fault-tolerant magnonic devices such as a spin-wave current splitter and a magnonic Fabry-Perot interferometer as discussed below.

The chiral spin-wave edge modes studied in this paper can be easily twisted or split by changes of the size (λ) and shape (r) of the unit cell, which we demonstrate in Figs. 7(a) and 7(b). In Fig. 7(a), the MC in phase II ($r = 1$) is connected with the other MC in phase III ($r > 1$), whose Chern integer for the lowest band differs by unit. A boundary between these two MC systems supports the chiral spin-wave edge mode which runs across the direct band gap at the $(0,\pi)$ point. This means that the two chiral edge modes propagating along the boundary of the the MC in phase II ($r = 1$) are spatially divided into two, where one mode goes along the boundary of the MC in the phase III ($r > 1$), while the other goes along the boundary between these two MCs. This configuration realizes a spin-wave current splitter, an alternative to those proposed in other geometries.[59]

The Fabry-Perot interferometer is made up of a couple of chiral spin-wave edge modes encompassing a single topological MC [see Fig. 7(c)]. Parts of the MCs are spatially constricted by the hole inside, so as to play a role of the point contact between these edge modes.[60] A unidirectional spin-wave propagation is induced in a chiral mode via either an antenna attached to the boundary ["input" in Fig. 7(c)] or a microwave-spin-wave transducer put near the boundary.[52,61] The wave is divided into two chiral edge modes at a point contact [PC1 in Fig. 7(c)]. Two chiral propagations merge into a single chiral propagation at the other point contact (PC2). Depending on a phase difference between these two, the superposed wave exhibits either a destructive or a constructive interference, which is detected as an electric signal from the other antenna ("output"). Note that local application of magnetic fields [PS1 or PS2 in Fig. 7(c)] changes the velocities of the two chiral edge modes locally. These modifications result in phase shifts of the two chiral waves, which thus changes the interference pattern observed in the output signal. With the use of these local magnetic fields as an external control,[20,62] the interferometer can serve as a solid-state based magnonic logic gate. A combination with a recently proposed resonant microwave-to-spin-wave transducer[61] would also expand further prospects of spintronic applications of these spin-wave devices.

Though chiral edge modes are robust against static perturbations, magnetic energies excited in the edge mode decay into either phonon states or other magnon states in the volume modes via inelastic scatterings. The associated decay time or coherence length depends on specific materials, and spin-wave propagation along the chiral edge mode survives only within this coherence length. Due to the absence of conduction electrons, however, spin waves in magnetic insulators have long coherence lengths; the coherence length in YIG in the magnetostatic regime becomes on the order of centimeter.[21] In such magnetic insulators, the characteristic spin-wave propagations depicted in Figs. 7(a)–7(c) are experimentally realizable especially in sizable MC systems. Experimental measurement of these propagations in the space- and time-resolved manner is by itself remarkable, which surely leads to the development of innovative spintronic devices in the future.

Note added. After submission of an original version of the present paper into the preprint server,[63] we found another submission,[64] which also theoretically explored the realization of a similar topological chiral magnonic edge mode in a localized spin system. Their edge modes come from the short-ranged Dzyaloshinskii-Moriya exchange interaction instead of the (more classical) magnetic dipole-dipole interaction studied here.

ACKNOWLEDGMENTS

We would like to thank M. Hashisaka for discussions. R.S. also thanks T. Momoi for informing him of Ref. 33. This work was supported in part by Grant-in-Aids from the Ministry of Education, Culture, Sports, Science and Technology of Japan (Grants No. 21000004, No. 22540327, No. 23740284, and No. 24740225) and by a Grant for Basic Scientific Research Projects from the Sumitomo Foundation.

APPENDIX: MAGNETIC MONOPOLE AND DIRAC HAMILTONIAN

When two bosonic (magnonic) bands form a band-touching point in the three-dimensional $\boldsymbol{p}$-parameter space with $\boldsymbol{p} \equiv (k_x,k_y,\lambda)$, the dual magnetic fields for these two bands [Eqs. (9), (28), and (29)] have a quantized source of their divergence at the point ($\boldsymbol{p} = \boldsymbol{p}_c$). Away from the band-touching point, the dual gauge fields [Eqs. (9) and (29)] can be locally determined, so that the dual magnetic fields [Eq. (28)] are clearly divergence free. At $\boldsymbol{p} = \boldsymbol{p}_c$ the projection to each of these two bands cannot be defined, which endows the respective dual magnetic field with some singular structure. The singular structure can be studied by the degenerate perturbation theory for a generalized eigenvalue problem. The eigenvalue problem takes a form

$$\boldsymbol{H}_{\boldsymbol{p}}\boldsymbol{T}_{\boldsymbol{p}} = \boldsymbol{\sigma}_3\boldsymbol{T}_{\boldsymbol{p}}\begin{bmatrix} \boldsymbol{E}_{\boldsymbol{p}} & \\ & -\boldsymbol{E}_{\overline{\boldsymbol{p}}} \end{bmatrix},$$

with $\boldsymbol{p} \equiv (k_x,k_y,\lambda)$ and $\overline{\boldsymbol{p}} \equiv (-k_x,-k_y,\lambda)$. The diagonal matrix $\boldsymbol{\sigma}_3$ takes $+1$ for the particle space while it takes -1 in the hole space. $\boldsymbol{H}_{\boldsymbol{p}}$ is a quadratic form of the boson Hamiltonian introduced in Sec. I. $\boldsymbol{E}_{\boldsymbol{p}}$ is a diagonal matrix, whose elements give dispersions for bosonic (magnonic) bands and are physically all positive definite. We decompose this into the zeroth-order part and the perturbation part,

$$\boldsymbol{H}_{\boldsymbol{p}} = \boldsymbol{H}_0 + \boldsymbol{V}_{\boldsymbol{p}} \tag{A1}$$

with $\boldsymbol{H}_0 \equiv \boldsymbol{H}_{\boldsymbol{p}=\boldsymbol{p}_c}$ and $\boldsymbol{V}_{\boldsymbol{p}} \equiv \boldsymbol{H}_{\boldsymbol{p}} - \boldsymbol{H}_0$. Suppose that $\boldsymbol{H}_0$ has twofold degenerate eigenstates $\boldsymbol{t}_j$ $(j = 1,2)$ with its eigenfrequency $\omega_0(> 0)$,

$$\boldsymbol{H}_0\boldsymbol{t}_j = \boldsymbol{\sigma}_3\boldsymbol{t}_j\omega_0,$$

where the states are normalized as $\boldsymbol{t}_j^{\dagger}\boldsymbol{\sigma}_3\boldsymbol{t}_m = \delta_{jm}$. On introducing the perturbation $\boldsymbol{V}_{\boldsymbol{p}}$, the degeneracy is split into two frequency levels. The eigenstate for the respective eigenfrequency is determined on the zeroth order of $\boldsymbol{p} - \boldsymbol{p}_c$ as

$$\boldsymbol{T}_{\boldsymbol{p}} = \boldsymbol{T}_0\boldsymbol{U}_{\boldsymbol{p}} + \mathcal{O}(|\boldsymbol{p} - \boldsymbol{p}_c|), \tag{A2}$$

where $\boldsymbol{T}_0$ diagonalizes $\boldsymbol{H}_0$ with $\boldsymbol{T}_0^{\dagger}\boldsymbol{\sigma}_3\boldsymbol{T}_0 = \boldsymbol{T}_0\boldsymbol{\sigma}_3\boldsymbol{T}_0^{\dagger} = \boldsymbol{\sigma}_3$ and a unitary matrix $\boldsymbol{U}_{\boldsymbol{p}}$ diagonalizes a 2 by 2 Hamiltonian $\boldsymbol{V}_{\text{eff}}$ formed by the twofold degenerate eigenstates,

$$\boldsymbol{V}_{\text{eff}} \equiv \begin{bmatrix} \boldsymbol{t}_1^{\dagger}\boldsymbol{V}_{\boldsymbol{p}}\boldsymbol{t}_1 & \boldsymbol{t}_1^{\dagger}\boldsymbol{V}_{\boldsymbol{p}}\boldsymbol{t}_2 \\ \boldsymbol{t}_2\boldsymbol{V}_{\boldsymbol{p}}\boldsymbol{t}_1 & \boldsymbol{t}_2^{\dagger}\boldsymbol{V}_{\boldsymbol{p}}\boldsymbol{t}_2 \end{bmatrix}. \tag{A3}$$

By substituting Eq. (A2) into Eqs. (9), (28), and (29), one can easily see that near $\boldsymbol{p} = \boldsymbol{p}_c$, the dual magnetic field is given only by the unitary matrix; in the leading order of $\boldsymbol{p} - \boldsymbol{p}_c$, it is given as

$$\boldsymbol{B}_j = \nabla \times \boldsymbol{A}_j + \mathcal{O}(|\boldsymbol{p} - \boldsymbol{p}_c|^{-1}), \ \ \boldsymbol{A}_j = i\text{Tr}[\boldsymbol{\Gamma}_j\boldsymbol{U}_{\boldsymbol{p}}^{\dagger}\nabla\boldsymbol{U}_{\boldsymbol{p}}],$$

with $\nabla \equiv (\partial_{k_x},\partial_{k_y},\partial_{\lambda})$. Now that Eq. (A3) reduces to a usual 2 by 2 Dirac-type Hamiltonian, we can show the quantization of the dual magnetic charge at the band-touching point exactly in the same way as in the 2 by 2 Dirac fermion system.[41,42] Thereby, the sign and the strength of the magnetic charge is determined only by the 2 by 2 effective Dirac Hamiltonian. With a proper gauge transformation and scale transformation, the effective Hamiltonian at the band-touching points P_j $(j = 1,2)$ takes a form

$$\mathcal{H}_{\text{eff}} = \omega_0\boldsymbol{\tau}_0 + (\lambda - \lambda_{c,j})\boldsymbol{\tau}_3 + ap_x\boldsymbol{\tau}_1 + bp_y\boldsymbol{\tau}_2,$$

with $a > 0$, $b > 0$, $(p_x,p_y) \equiv (k_x - \pi,k_y)$ for $j = 1$ and $(p_x,p_y) \equiv (k_x,k_y - \pi)$ for $j = 2$. Equation (30) is derived by the replacement of $p_{\mu} \to -i\partial_{\mu}$.

[*] Present address: International Center for Quantum Materials (ICQM), Peking University, No. 5 Yiheyuan Road, Haidian District, Beijing, 100871, China.

[1] C. L. Kane and E. J. Mele, Phys. Rev. Lett. **95**, 226801 (2005).

[2] C. L. Kane and E. J. Mele, Phys. Rev. Lett. **95**, 146802 (2005).

[3] B. A. Bernevig and S. C. Zhang, Phys. Rev. Lett. **96**, 106802 (2006).

[4] B. A. Bernevig, T. L. Hughes, and S. C. Zhang, Science **314**, 1757 (2006).

[5] L. Fu, C. L. Kane, and E. J. Mele, Phys. Rev. Lett. **98**, 106803 (2007).

[6] M. König, S. Wiedmann, C. Brune, A. Roth, H. Buhmann, L. W. Molenkamp, X. L. Qi, and S. C. Zhang, Science **318**, 766 (2007).

[7] D. Hsieh, D. Qian, L. Wray, Y. Xia, Y. S. Hor, R. J. Cava, and M. Z. Hasan, Nature (London) **452**, 970 (2008).

[8] X. L. Qi, T. L. Hughes, and S. C. Zhang, Phys. Rev. B **78**, 195424 (2008).

[9] N. Read and D. Green, Phys. Rev. B **61**, 10267 (2000).

[10] D. A. Ivanov, Phys. Rev. Lett. **86**, 268 (2001).

[11] J. Jang, D. G. Ferguson, V. Vakaryuk, R. Budakian, S. B. Chung, P. M. Goldbart, and Y. Maeno, Science **331**, 186 (2011).

[12] Y. Aoki, Y. Wada, M. Saitoh, R. Nomura, Y. Okuda, Y. Nagato, M. Yamamoto, S. Higashitani, and K. Nagai, Phys. Rev. Lett. **95**, 075301 (2005).

[13] A. Y. Kitaev, Phys. Usp. **44**, 131 (2001).

[14] F. D. M. Haldane and S. Raghu, Phys. Rev. Lett. **100**, 013904 (2008).

[15] S. Raghu and F. D. M. Haldane, Phys. Rev. A **78**, 033834 (2008).

[16] C. Zhang and Q. Niu, Phys. Rev. A **81**, 053803 (2010).

[17] Z. Wang, Y. Chong, J. D. Joannopoulos, M. Soljačić, Nature (London) **461**, 772 (2009).

[18] R. W. Damon, and J. R. Eschbach, J. Phys. Chem. Solids **19**, 308 (1961).

[19] R. W. Damon and H. Van De Vaart, J. Appl. Phys. **36**, 3453 (1965).

[20] V. V. Kruglyak, S. O. Demokritov, and D. Grundler, J. Phys. D **43**, 264001 (2010).

[21] A. A. Serga, A. V. Chumak and B. HillebrandsJ. Phys. D **43**, 264002 (2010).

[22] B. Lenk, H. Ulrichs, F. Garbs, and M. Münzenberg, Phys. Rep. **507**, 107 (2011).

[23] Yu. V. Gulyaev, S. A. Nikitov, L. V. Zhivotovskii, A. A. Klimov, Ph. Tailhades, L. Presmanes, C. Bonningue, C. S. Tsai, S. L. Vysotskii, and Y. A. Filimonov, JETP Lett. **77**, 567 (2003).

[24] N. Singh, S. Goolaup, and A. O. Adeyeye, Nanotechnology **15**, 1539 (2004).

[25] C. C. Wang, A. O. Adeyeye, and N. Singh, Nanotechnology **17**, 1629 (2006).

[26] A. O. Adeyeye and N. Singh, J. Phys. D: Appl. Phys. **41**, 153001 (2008).

[27] B. A. Kalinikos and A. N. Slavin, J. Phys. C: Solid State Phys. **19**, 7013 (1986).

[28] J. O. Vasseur, L. Dobrzynski, B. Djafari-Rouhani, and H. Puszkarski, Phys. Rev. B **54**, 1043 (1996).

[29] M. Krawczyk and H. Puszkarski, Phys. Rev. B **77**, 054437 (2008).

[30] G. Sietsema, and M. E. Flatté, arXiv:1111.2506.

[31] R. Matsumoto and S. Murakami, Phys. Rev. Lett. **106**, 197202 (2011).

[32] R. Matsumoto and S. Murakami, Phys. Rev. B **84**, 184406 (2011).

[33] J. H. P. Colpa, Physica A **93**, 327 (1978).

[34] J. E. Avron, R. Seiler, and B. Simon, Phys. Rev. Lett. **51**, 51 (1983).

[35] D. J. Thouless, M. Kohmoto, M. P. Nightingale, and M. den Nijs, Phys. Rev. Lett. **49**, 405 (1982).

[36] M. Kohmoto, Ann. Phys. (N.Y.) **160**, 343 (1985).

[37] T. Holstein and H. Primakoff, Phys. Rev. **58**, 1098 (1940).

[38] T. Fukui, Y. Hatsugai, and H. Suzuki, J. Phys. Soc. Jpn. **74**, 1674 (2005).

[39] M. Karplus and J. M. Luttinger, Phys. Rev. **95**, 1154 (1954).

[40] M. Onoda and N. Nagaosa, J. Phys. Soc. Jpn. **71**, 19 (2002).

[41] M. V. Berry, Proc. R. Soc. London, Ser. A **392**, 45 (1984).

[42] B. Simon, Phys. Rev. Lett. **51**, 2167 (1983).

[43] W. P. Su, J. R. Schrieffer, and A. J. Heeger, Phys. Rev. Lett. **42**, 1698 (1979).

[44] A. J. Niemi, and G. W. Semenoff, Phys. Rep. **135**, 99 (1986).

[45] S. Neusser, B. Botters, and D. Grundler, Phys. Rev. B **78**, 054406 (2008).

[46] S. Neusser, B. Botters, M. Becherer, D. Schmitt-Landsiedel, and D. Grundler, Appl. Phys. Lett. **93**, 122501 (2008).

[47] S. Tacchi *et al.*, IEEE Trans. Magn. **46**, 172 (2010).

[48] G. Gubbiotti, S. Tacchi, M. Madami *et al.*, Appl. Phys. Lett. **100**, 162407 (2012).

[49] S. Demokritov, B. Hillebrands, and A. N. Slavin, Phys. Rep. **348**, 442 (2001).

[50] M. Bauer, O. Buttner, S. O. Demokritov, B. Hillebrands, V. Grimalsky, Y. Rapoport, and A. N. Slavin, Phys. Rev. Lett. **81**, 3769 (1998).

[51] B. Hillebrands, Rev. Sci. Instrum. **70**, 1589 (1999).

[52] Y. Au, T. Davison, E. Ahmad, P. S. Keatley, R. J. Hicken, and V. V. Kruglyak, Appl. Phys. Lett. **98**, 122506 (2011).

[53] Geisau, O. V. Netzelmann, U. Rezende, and S. M. J. Pelzl, IEEE Trans. Magn. **26**, 1471 (1990).

[54] N. P. Vlannes, J. Appl. Phys. **61**, 416 (1987).

[55] R. Shindou, J. I. Ohe, R. Matsumoto, S. Murakami, and E. Saitoh, Phys. Rev. B **87**, 174402 (2013).

[56] Y. Kajiwara, K. Harii, S. Takahashi, J. Ohe, K. Uchida, M. Mizuguchi, H. Umezawa, H. Kawai, K. Ando, K. Takanashi, S. Maekawa, and E. Saitoh, Nature (London) **464**, 262 (2010).

[57] Y. Dvornik Au and V. V. Kruglyak, *Topics in Applied Physics*, edited by S. O. Demokritov and A. N. Slavin (Springer, Berlin, 2013), Vol. 125, p. 101.

[58] B. I. Halperin, Phys. Rev. B **25**, 2185 (1982).

[59] V. E. Demidov, J. Jersch, K. Rott, P. Krzysteczko, G. Reiss, and S. O. Demokritov, Phys. Rev. Lett. **102**, 177207 (2009).

[60] Y. Ji, Y. Chung, D. Sprinzak, M. Heiblum, D. Mahalu, and H. Shtrikman, Nature (London) **422**, 415 (2003).

[61] Y. Au, E. Ahmad, O. Dmytriiev, M. Dvornik, T. Davison, and V. V. Kruglyak, Appl. Phys. Lett. **100**, 182404 (2012).

[62] T. Schneider, A. A. Serga, B. Leven, B. Hillebrands, R. L. Stamp, and M. P. Kostylev, Appl. Phys. Lett. **92**, 022505 (2008).

[63] R. Shindou, R. Matsumoto, and S. Murakami, arXiv:1204.3349.

[64] L. Zhang, J. Ren, J.-S. Wang, and B. Li, Phys. Rev. B **87**, 144101 (2013).